Title page

A Novel Mouse Model for *LAMA2*-Related Muscular Dystrophy: Analysis of Molecular Pathogenesis and Clinical Phenotype

Dandan Tan[1, 7], Yidan Liu[1], Huaxia Luo[1], Qiang Shen[2], Xingbo Long[3], Luzheng Xu[4], Jieyu Liu[1], Nanbert Zhong[5,*], Hong Zhang[2,*] & Hui Xiong[1, 6,*]

***Correspondence**

Hui Xiong, M.D., PhD., Department of Pediatrics, Peking University First Hospital, Beijing, 100034, China. Tel.: +8610-83573238; Email: xh_bjbj@163.com

Hong Zhang, PhD., Institute of Cardiovascular Sciences and Key Laboratory of Molecular Cardiovascular Sciences, Peking University Health Science Center, Beijing, 100191, China. Tel.: +8610-82801510; Email: zhanghong@bjmu.edu.cn

Nanbert Zhong, M.D., New York State Institute for Basic Research in Developmental Disabilities, 1050 Forest Hill Road, Staten Island, NY 10314, USA. Tel/Fax: +1 718 494 5242/4882; E-mail: nanbert.zhong@opwdd.ny.gov

Author affiliations

[1]Department of Pediatrics, Peking University First Hospital, Beijing, 100034, China

[2]Institute of Cardiovascular Sciences and Key Laboratory of Molecular Cardiovascular Sciences, Peking University Health Science Center, Beijing, 100191, China

[3]Department of Urology, Sun Yat-sen University Cancer Center, Guangzhou, Guangdong, 510060, China

[4]Medical and Health Analysis Center, Peking University, Beijing, 100191, China

[5]New York State Institute for Basic Research in Developmental Disabilities, 1050 Forest Hill Road, Staten Island, NY 10314, USA

[6]Beijing Key Laboratory of Molecular Diagnosis and Study on Pediatric Genetic Diseases, Beijing 100034, China

[7]Department of Neurology, the First Affiliated Hospital of Nanchang University, Nanchang, Jiangxi, 330006, China

Acknowledgments

The authors would like to express their gratitude to Dr. Ching H. Wang for his critical reading and editing of this manuscript and Dr. Y. Zhu for his assistance in the analysis of the RNA sequencing data. This study received support from the following grants: National High Level Hospital Clinical Research Funding (High Quality Clinical Research Project of Peking University First Hospital) (No. 2022CR69 to H.X.), National Natural Science Foundation of China (No. 82171393 to H.X.), Natural Science Foundation of Beijing Municipality (No. 7212116 to H.X.), National Key Research and Development Program of China (No. 2016YFC0901505 to H.X.), Beijing Key Laboratory of Molecular Diagnosis and Study on Pediatric Genetic Diseases (No. BZ0317 to H.X.), and Research Foundation for Youth Talents of the First Affiliated Hospital of Nanchang University (No. YFYPY202223 to D.T.).

Author contributions

D.T. performed the experiments, analyzed the data, and drafted the manuscript. Y.L. participated in performing the experiments and analyzing the data. H. L. participated in analyzing the single cell sequencing data and contributed to the drafting of the manuscript. Q.S. conducted hematoxylin and eosin (H&E) and Sirius Red staining on mouse muscles. X.L. participated in analyzing the RNA sequencing data and contributed to the drafting of the manuscript. L.X. assisted with the muscle MRI and contributed to the drafting of the manuscript. J.L. performed immunohistochemistry assay on human muscles. H.Z. guided the experiments, analyzed the mouse phenotype data and revised the manuscript. H.X. and N.Z. designed the study, analyzed the data, and contributed to the drafting, reviewing, and finalizing of the manuscript. All authors read and approved the final manuscript.

Author Approvals

All authors have seen and approved the manuscript, and that it hasn't been accepted or published elsewhere.

Competing interests

The authors declare no competing interests.

Ethics

All procedures were approved by the Animal Ethics Committee of Peking University First Hospital (J202027) and followed the guidelines of the Care and Use of Laboratory Animals.

Data availability

The datasets generated during this study are available from the corresponding authors on reasonable request.

Abstract

Understanding the underlying pathogenesis of *LAMA2*-related muscular dystrophy (*LAMA2*-MD) have been hampered by lack of genuine mouse model. We created a new *Lama2* knockout mouse (dy^H/dy^H) and reported here its close simulation to human neuropathology and symptoms. We first established that *Lama2* was predominantly expressed within the cortical surface of normal mouse brain, specifically, highly concentrated in vascular and leptomeningeal fibroblasts and vascular smooth muscle cells with a modest presence within astrocytes. Our *Lama2* knockout mice confirmed specific decreased *Lama2* expression in those cell types and resulted in disruption of gliovascular basal lamina assembly. This molecular pathogenesis mechanism was elucidated by a novel scRNA-seq. Furthermore, through transcriptomic investigation, these dy^H/dy^H mice were showed aberrant structure of muscle cytoskeletons which impaired normal muscle development and resulted in weakness. This is the first reported genuine model simulating human *LAMA2*-MD. We can use it to study the molecular pathogenesis and develop effective therapies.

Keywords: Single cell RNA sequencing; Transcriptomic study; Novel mouse model; *Lama2*; Muscular dystrophy; Blood-brain barrier

Introduction

LAMA2-related muscular dystrophy (*LAMA2*-MD), caused by pathogenic variants in the *LAMA2* gene, is an autosomal recessive disorder characterized by varying degrees of muscle weakness and abnormal brain white matter hyperintensities on T2-weighted magnetic resonance imaging (MRI) (*Zambon et al., 2020*). The clinical features of *LAMA2*-MD can be divided into two subgroups: 1. severe, early-onset *LAMA2*-related congenital muscular dystrophy (*LAMA2*-CMD, OMIM 607855), and 2. mild, late-onset autosomal recessive limb-girdle muscular dystrophy-23 (LGMDR23, OMIM 618138) (*Tan D et al., 2021*). *LAMA2*-MD has an estimated prevalence of 4 in 500,000 children (*Nguyen et al., 2019*), and accounts for 36-48% of all patients diagnosed with congenital muscular dystrophies (CMDs) (*Sframeli et al., 2017; Abdel Aleem et al., 2020; Ge et al., 2019*). Dystrophic muscle pathology and clinical motor weakness are the common characteristics of *LAMA2*-MD patients. Nearly all patients also exhibit abnormal cortical white matter shown in T2 images of brain MRI. Some patients have associated brain dysfunctions such as seizures and cognitive delay with variable degrees of cerebral dysgenesis such as occipital pachygyria (*Tan D et al., 2021*). It was suspected that Laminin α2 deficiency was associated with the disruption of basement membrane formation and the aberrant gliovascular basal lamina assembly which resulted in abnormal development of blood-brain barrier (*Gawlik and Durbeej, 2020; Menezes et al., 2014; Arreguin and Colognato, 2020*). These anomalies also interfere with cellular mechanical linkage and signal transductions between cortical neurons. Similar pathogenesis has been speculated to be occurring in skeletal muscles and the failure of sarcolemma stability resulted in dystrophic changes and contractile dysfunction in these muscle cells. However, the true molecular mechanisms underlying the pathogenesis of muscular dystrophy and the associated brain dysfunctions in *LAMA2*-MD remain largely unknown.

The *LAMA2* gene (OMIM 156225) is located on chromosome 6q22.33, spanning 65 exons and encodes the laminin α2 chain, which is predominantly expressed in skeletal muscle cells, astrocytes and pericytes of brain capillaries, as well as Schwann cells of peripheral nerves (*Mohassel et al., 2018*). Laminin α2 connects with laminin β1 and γ1 chains to form a heterotrimeric protein laminin-α2β1γ1 (LM-211), which is responsible for the basement membrane assembly (*Yurchenco et al., 2018*). LM-211 anchors to two major groups of receptors on the cell surface, α-dystroglycan and integrins (α1β1, α2β1, α6β1, α7β1), to form dystroglycan-matrix scaffolds and regulate signal transductions for cell adhesion, migration and differentiation (*Hoheneste, 2019; Durbeej, 2010; Aumailley, 2021*).

In our previous study, we discovered that variants in exons 3-4 region of the *LAMA2* gene is the most

frequent occurrence in patients with *LAMA2*-MD (*Yurchenco et al., 2018; Ge et al., 2018*). Building on this discovery, we utilized clustered regularly interspaced short palindromic repeats (CRISPR)-Cas9 gene editing technology to specifically delete exon 3 of the *Lama2* gene, creating a novel *Lama2* knockout (KO) mouse model for *LAMA2*-MD, named 'dy^H/dy^H'. We first investigated the histopathological findings in the brain and muscle of these dy^H/dy^H mice. We then studied their molecular pathogenetic mechanisms by conducting single-cell RNA sequencing (scRNA-seq) to monitor the molecular changes occurred in the various cell types of the brains. We also performed RNA sequencing on muscle tissues in the dy^H/dy^H mice and conducted phenotype analyses including motor strength testing to correlate the molecular alterations with the muscle pathology and their motor dysfunction.

Results

dy^H/dy^H mice: A novel mouse model for *LAMA2*-MD

We have created a new mouse model dy^H/dy^H for human *LAMA2*-MD that closely simulates human neuropathology and clinical phenotype (**Figure 1**). This was achieved by targeted removal of exon 3 from the mouse *Lama2* gene utilizing CRISPR-Cas9 gene editing technology (*Barazesh et al., 2021*). To assess the phenotype of these *Lama2* KO mice, we recorded the general appearance, body weight, life span and motor function of wild-type (WT), heterozygote (Het, $dy^H/+$), and homozygous dy^H/dy^H progenies (**Figure 2**). The dy^H/dy^H mice were smaller and thinner when compared with the WT and Het mice. They had delayed weight gain when observed at postnatal days 7 (P7) and worsened through P10 to P24. Kaplan–Meier survival analysis revealed that the median survival of dy^H/dy^H mice was 21 days (ranged from 12 to 35 days) while WT and Het mice remained in good health throughout the observation period of one year. The $dy^{H/}dy^H$ mice exhibited reduced activity and quiescent behavior. At postnatal day 7 (P7), the dy^H/dy^H mice experienced challenges in maintaining an upright stance and difficulty righting from supine. By P14, these mice were not only less active and smaller than their WT counterparts but also displayed significant weakness. This weakness progressed rapidly, reaching a debilitating state at around 3-4 weeks of age. This progression of symptoms and decline in motor function is evident. The average four-limb grip strength of the dy^H/dy^H mice exhibited slow initial improvement over the course of 21 days post birth, followed by a subsequent decline. Their grip strength remained consistently lower than that of the WT mice at all assessment time points (P10, P14, P17, P21 and P24) (**Figure 2A**). During the period from P18 to P24, the dy^H/dy^H mice demonstrated inferior performance on the treadmill compared to the WT mice. This was reflected in a significantly higher frequency of receiving electric shocks in the dy^H/dy^H mice compared to their WT counterparts at P18 to P24 (**Figure 2A**). These

observations collectively indicate a severe phenotype in the dy^H/dy^H mice, characterized by diminished body weight, profound muscle weakness, and a shortened lifespan.

To further investigate the muscle pathology of the dy^H/dy^H mice, we measured the serum creatine kinase (CK) levels, conducted muscle magnetic resonance imaging (MRI) studies, and performed muscle histopathological analyses.

1. Serum CK: The mean serum CK levels were significantly elevated in dy^H/dy^H mice when compared to the WT mice at both postnatal days 14 (P14) and 21 (P21), reaching approximately 9-10 times at the highest levels. There was no discernible difference in serum CK levels between WT and heterozygous (Het) mice (**Figure 2A**).
2. Muscle MRI: Pelvic and hindlimb muscle MRI scans showed significant discrepancies in muscle volume. On T1-weighted MRI, dy^H/dy^H mice displayed substantially smaller muscle volumes. Additionally, on T2-weighted MRI images, there were significantly increased hyperintense regions in dy^H/dy^H muscles when compared to their age-matched WT counterparts at both P14 and P21 (**Figure 2B**).
3. Muscle histopathology: Examination of biceps femoris muscle sections revealed increased variation in fiber size at P7 of dy^H/dy^H mice. At P14, the muscle pathology assessment indicated severe dystrophic changes including muscle fiber degeneration, necrosis, and regeneration. There was significant increase in connective tissue infiltration and inflammation within dy^H/dy^H muscles (**Figure 3**). Similar dystrophic features were observed in other muscles including quadriceps femoris, gastrocnemius, triceps brachii, diaphragm, and tongue, though to a lesser extent in the biceps femoris. Notably, heart and intestinal muscles appeared to be spared from such changes (**Figure 4A**). Western blot analysis of unreduced muscle extracts from dy^H/dy^H mice revealed the absence of the 300 kDa laminin α2 and the 700 kDa cross-linked LM-211 complex protein. These observations strongly indicate a complete loss of laminin α2 protein in dy^H/dy^H mice (**Figure 4B**). Immunofluorescence staining further confirmed the deficiency of laminin α2 within muscle tissue of dy^H/dy^H mice (**Figure 4C**).

These findings collectively provided evidence for the severe CMD phenotype in our dy^H/dy^H mice and established the first genuine murine model for human *LAMA2*-CMD.

Disruption of blood-brain barrier in dy^H/dy^H mouse brain

The blood-brain barrier (BBB) is composed of several cell types, including microvascular endothelial cells, pericytes, astrocytes, vascular smooth muscle cells, and the basement membrane (*Villanova et al., 1997; Villanova et al., 1996; Hagg et al., 1997*). These components along with microglia collectively form the structure known as the neurovascular unit. Previous studies have indicated that laminin α2 is prominently expressed in astrocytes and pericytes, and it is primarily localized to the basal lamina of cerebral blood vessels

in the adult human brain.

To study the molecular mechanisms underlying the brain abnormalities in the dy^H/dy^H mice, we conducted a comprehensive analysis of laminin α2 expression on the brains of dy^H/dy^H (KO) and compared it with WT mice at P14. This investigation employed single-cell RNA sequencing (scRNA-seq) to compare the transcriptional profiles between dy^H/dy^H and WT mouse brains. A total of 8,111 cells from dy^H/dy^H mouse brain and 8,127 cells from WT mouse brain were captured using the 10X Genomics platform. The cell clusters within both dy^H/dy^H and WT brains were annotated through aggregation of the sequencing data that resulted in the classification of these clusters into three major categories: neuronal cells, glial cells, and non-neuronal cells. Fifteen distinct clusters were identified with marker genes, including clusters associated with hippocampal neurons (Hippo-neuron), glutamatergic neurons (Glu-neuron), GABAergic neurons (GABA-neuron), neuron-glial antigen 2 neurons (NG2-neuron), neuron-C5, astrocytes (Astro), cerebellum glia cells (CGC), oligodendrocytes (Oligo), microglia (Micro), vascular and leptomeningeal fibroblasts (VLF), vascular smooth muscle cells (VSM), choroid plexus cells (CPC), ependymal cells (Epen), endothelial cells (Endo), and macrophages (Macro) (**Figure 5A, B**). The comparative analysis of cell clusters between the dy^H/dy^H and WT brains revealed a notable increase in the proportion of GABAergic neurons and a decrease in astrocytes and glutamatergic neurons in the dy^H/dy^H brain (**Figure 5C**).

To ascertain which cell types express laminin α2, we conducted RNA sequencing analysis to measure the *Lama2* expression within each cell cluster. The findings revealed that in WT mouse brain, *Lama2* exhibited selective and robust expression in vascular and leptomeningeal fibroblasts and vascular smooth muscle cells with a low level of expression in astrocytes (**Figure 5D**). Of note, *Lama2* was selectively expressed in some special types of astrocytes. This finding was further corroborated by immunofluorescence analysis, which confirmed the predominant expression of laminin α2 on the cortical surface of WT mice at P14 (**Figure 5E**). This evidence confirmed that laminin α2 is a crucial component of the gliovascular basal lamina within the BBB.

Analysis of differentially expressed genes (DEGs) was conducted within each cell cluster, comparing the dy^H/dy^H and WT brains to uncover the aberrant transcriptional patterns across various cell types in the dy^H/dy^H mouse brain. As anticipated, *Lama2* expression was found to be significantly diminished in vascular and leptomeningeal fibroblasts, vascular smooth muscle cells, and astrocytes in the dy^H/dy^H brain (**Figure 5D**). The genes showing differential expression were subjected to analysis using Gene Ontology (GO) terms, revealing enrichment in several extracellular matrix processes within vascular and leptomeningeal fibroblasts. For

vascular smooth muscle cells, the DEGs were associated with the pathway of cytoplasmic side of the membrane, axon and astrocyte projections (**Figure 5F**).

Immunofluorescence staining showed a reduced expression of GFAP only in the leptomeningeal (**Figure 5C, E**). Combined with scRNA-seq showed *Lama2* was selectively expressed in certain types of astrocytes, this further confirmed that Lama2 deficiency affected astrocytes such as radial neuroglia cells which involved in the gliovascular basal lamina. These findings collectively pointed towards potential disruptions in the structure and function of the blood-brain barrier and pia mater as a consequence of *Lama2* knocked-out, suggesting an underlying impact on BBB integrity and possibly affecting the pia mater's normal function.

To delve into the alterations within the intricate network of the brain, particularly the BBB, cell-cell communications were predicted by CellChat V1.6, a tool which quantitatively inferred and analyzed intercellular communication networks from scRNA-seq data (*Jin et al., 2021*). Upon a more detailed investigation of communications among different cell populations, it was found that the distribution of communications between dy^H/dy^H and WT was largely similar. Notably, the most robust communications were observed between vascular and leptomeningeal fibroblasts and astrocytes, and communications involving vascular and leptomeningeal fibroblasts were generally high (**Figure 5G**). Although the overall distribution and strength of communications were not significantly different between dy^H/dy^H and WT, noticeable differences were observed in communications associated with the laminins' pathway. Notably, pairs involving *Lama2*, and its receptors were present only in WT, whereas ligand-receptor pairs related to *Lama1* were exclusively observed in dy^H/dy^H. Moreover, several pairs demonstrated higher communication levels in dy^H/dy^H than in WT (**Figure 6A**). These findings suggested that the loss of communications associated with laminin α2, which mediates connections between the extracellular matrix and cell membranes, led to the activation of compensatory communications within other laminin pathways. Significant differences in cell-cell communications were particularly evident in pairs involving vascular and leptomeningeal fibroblast-astrocyte, vascular and leptomeningeal fibroblast-vascular smooth muscle cell, vascular and leptomeningeal fibroblast-endothelial cell, and vascular and leptomeningeal fibroblast-cerebellum glia cell pairs (**Figure 6A**).

We also found that several genes expressed differently across more than 5 cell clusters (**Figure 6B**). The expression levels of *Mbp*, *Mobp*, and *Plp1* were significantly reduced in multiple cell clusters within the dy^H/dy^H brain compared to the WT, suggesting potential disruptions in the formation or development of the myelin sheath. These changes could be linked to the abnormal brain white matter observed in human *LAMA2*-MD[2].Several genes implicated in transmembrane ionic transportation, regulation of synaptic transmission, and

maintenance of BBB homeostasis, also showed differential expression across several cell clusters (**Figure 6B**):

1. The expression of *Slc1a2*, associated with BBB transport, was significantly decreased in GABAergic neurons, vascular smooth muscle cells, and choroid plexus cells in dy^H/dy^H compared to WT.
2. The expression of *Mt3*, involved in transmembrane ionic transportation was significantly decreased in glutamatergic neurons, GABAergic neurons, vascular smooth muscle cells, and macrophages within dy^H/dy^H compared to WT.
3. The expression of *Slc6a13*, involved in synaptic transmission, was notably increased in vascular and leptomeningeal fibroblasts of dy^H/dy^H mice.

In conclusion, these scRNA-seq analysis findings indicated that the loss of laminin α2 in vascular and leptomeningeal fibroblasts, vascular smooth muscle cells, and astrocytes contributed to the disruption of the BBB integrity. These findings also provided substantial evidence for the dysfunction of glutaminergic- and GABAergic neuronal systems and the disruptions of ionic homeostasis in the brain of dy^H/dy^H mouse brain caused by the loss of laminin α2.

Impaired muscle cytoskeleton and muscle development in dy^H/dy^H mice

In previous studies of *LAMA2*-MD (*Nguyen et al., 2019; Gawlik and Durbeej, 2020*), the focus on the pathogenesis of muscular dystrophy was primarily concentrated on the secondary histopathological changes such as fibrosis, inflammation, apoptosis, and metabolism. There was little attention given to the direct impact on muscle cytoskeleton and muscle development. The cytoskeletons form a complex and interconnected network that is crucial for maintaining both cellular contractility and mechanical stability of the muscle fibers. To further study the molecular mechanisms underlying the muscle pathology, we conducted a buck-cell RNA sequencing (bcRNA-seq) on biceps femoris muscles obtained from WT, heterozygote (Het, $dy^H/+$), and dy^H/dy^H (KO) mice at postnatal day 14 (P14). Principal component analysis (PCA), a technique used to reduce complex data to its principal components for visualization, demonstrated distinct patterns between dy^H/dy^H and WT muscle tissues (**Figure 7A**). A total of 2,020 DEGs were identified, with 1136 genes upregulated and 884 genes downregulated in the KO muscles compared to WT muscles. To pinpoint the biological pathways linked to the pathogenic mechanism in KO muscle tissues, we conducted gene set enrichment analyses (GSEA) using both Gene Ontology (GO) and the Kyoto Encyclopedia of Genes and Genomes (KEGG) databases (*Huang et al., 2022*). The GO function analysis demonstrated that the DEGs were notably enriched in muscle cytoskeleton, extracellular matrix, and cell membrane. They were particularly notable during muscle development, inflammation, apoptosis, and in the pathways of mitochondrial energy metabolism. To shed light on the

previously less understood aspects of dystrophic pathology, we particularly focused on the DEGs related to muscle cytoskeleton and development, which revealed a significant downregulation of several muscle cytoskeleton-related genes in KO mice. These genes included *Myh6*, *Myh7*, *Myl3*, *Myl2*, *Tuba8*, *Myoz3*, *Actc1*, *Mstn*, *Tppp*, *Mylk4*, *Mybpc2*, *Mrln*, *Mybph*, *Ckmt2*, *Myct1*, and *Abra* (**Figure 7B**). This downregulation collectively suggested an impairment of the muscle cytoskeleton in KO mice. Partial abnormal expressions of muscle cytoskeleton-related proteins were further assessed and validated by immunofluorescence and Western blot. There was focal and increased expression of MYHC (myosin heavy chain) observed through immunofluorescence in dy^H/dy^H muscles (**Figure 8**). This finding was further confirmed by significantly elevated levels of MYHC and MYH2 proteins detected by Western blot (**Figure 8**). Desmin and β-tubulin also exhibited focal increases in dy^H/dy^H muscles through immunofluorescence analysis, though no differences by Western blot analysis.

Further analysis of DEGs also revealed an upregulation in the expression of several myogenic regulatory factors (MRFs), including *Myog*, *Myof*, *Myo5a*, *Myh4*, *Myh3*, and *Myh8* in dy^H/dy^H muscles. Immunofluorescence analysis demonstrated focal increases in MYOG, MYOD1, and MYF5 in dy^H/dy^H muscles (**Figure 8**). However, Western blot analysis showed no significant differences in the total levels of MYOG and MYOD1 proteins within dy^H/dy^H muscles (**Figure 8**).

Considering that α-dystroglycan and integrins are the two major groups of receptors for LM-211, our investigation focused on the hypothesis that genes related to *Dag1* and integrins might display differential expression (*Hoheneste, 2019; Durbeej, 2010; Aumailley, 2021*). This led to the discovery of upregulated integrin-related genes, including *Itgal*, *Itgax*, *Itgam*, *Itgb2*, and *Itgb7*, within dy^H/dy^H muscles. Furthermore, protein-protein interaction analysis demonstrated a direct interaction between Lama2 and Itgb2, as well as Itgb7 (**Figure 7C**). However, in contrast to integrin-related genes, no differential expression of the Dag1 gene was observed, and α-dystroglycan levels detected by immunofluorescence showed no significant differences. Notably, a series of DEGs associated with cell membrane transport were also identified, further expanding the potential scope of muscle damage mechanisms. These genes included *Tmem52*, *Tmem106a*, *Tmem176a*, *Tmem176b*, *Tmem246*, *Tmem143*, *Tmem38a*, *Tmem233*, *Tmem177*, *Tmem25*, *Tmem37*, *Tmem86a*, *Tmem100*, *Tmem221*, *Tmem79*, and *Tmem178*. These findings suggested that the muscle damage in dy^H/dy^H mice could potentially be mediated by abnormal integrin signaling and altered transmembrane proteins, rather than α-dystroglycan. This observation aligns with the lack of differential expression of the Dag1 gene in both muscle and brain analyses, which might explain why dystroglycanopathies exhibit severe CNS symptoms and structural

malformations, including type II lissencephaly, whereas the CNS symptoms and brain structural malformations observed in *LAMA2*-MD are relatively mild.

These observations collectively support the disruptions in the development and regeneration of muscle fibers in dy^H/dy^H mice, as evidenced by the changes in the expression levels of key muscle development-related proteins.

Discussion

It has been several decades since the initial identification of human *LAMA2*-related muscular dystrophy. *LAMA2*-CMD is the most common CMD subtype worldwide. However, the underlying pathogenesis is still not clear and there is no effective treatment. Mouse models are essential tools for studying the pathogenic mechanism and developing therapeutic strategies for human muscular dystrophies and congenital myopathies (*Sztretye et al., 2020; van Putten et al., 2020*). Here, we generated a *LAMA2*-CMD mouse model by utilizing a CRISPR/Cas9 technology and based on the frequently observed disease-causing genetic variant in human patients. We describe the close simulation of their clinical phenotype with human *LAMA2*-CMD patients and provided detailed molecular genetic analysis of their pathogenetic mechanism.

From our transcriptomic expression studies, *Lama2* was selectively and highly expressed in vascular and leptomeningeal fibroblasts, and vascular smooth muscle cells, with a small amount of expression in astrocytes. Laminin α2 deficiency at pial surfaces and the blood-brain barrier (BBB) leads to BBB disruption and radial glial cells (RGCs) dysfunction. We also clearly demonstrated the cell types which expressed *Lama2* and provided evidence for the impaired gliovascular basal lamina of BBB (*Severino et al., 2020; Devisme et al., 2012*), which was associated with brain abnormalities in *LAMA2*-MD (**Figure 6C**). The observation of occipital pachygyria in human patients is most likely related to the impaired gliovascular basal lamina of BBB and occurrence of seizures in these patients could be related to the aberrant neuronal network formation and the imbalance of excitability and inhibitory neuronal network and ionic homeostasis (*Barkovich et al., 2015; Jayakody et al., 2020; Sarkozy et al., 2020; Huang et al., 2023*). This disturbance of ionic homeostasis might result in the accumulation of interstitial fluid within the myeline sheath and observed in the T2 hyperintensity in the brain MRI.

Ontogenic observations of muscle development from early to late postnatal periods provide detailed understanding of pathogenic processes in human muscular disorders. In this study, we observed significant fiber size variations in the muscles of dy^H/dy^H mice as early as P7. The typical dystrophic changes, fibrosis and inflammation accelerated until P14 and then decelerated until they expired. Muscle pathology with

inflammation and fibrosis assessed by muscle MRI was previously reported in dy^w/dy^w mice at the age of 7 weeks (*Vohra et al., 2015*). In this study, muscle MRI was performed much earlier (age of 2-3 weeks) in dy^H/dy^H mice and showed a decreased muscle volume due to muscle wasting on T1-weighted MRI and abnormal hyperintense pixels for inflammation on T2-weighted MRI. These results were consistent with muscle pathology and indicated that muscle MRI could be a useful, sensitive and reliable method for monitoring changes in muscle pathology of muscular dystrophies in preclinical research (*Porcari et al., 2020; Decostre et al., 2013*).

Muscle pathological events from the early postnatal stage to the last stage could provide a better understanding of the development of muscle damage and pathology with disease progression (*Mehuron et al., 2014; Durbeej, 2015; Gawlik et al., 2017*). In addition to the limb muscles, the diaphragm and glossal muscles were involved, indicating extensive muscle dystrophic change in dy^H/dy^H mice, which was consistent with those previously observed in dy^{3k}/dy^{3k} mice (*Gawlik et al., 2019*). The extensive involvement of muscle pathology resulted in low body weight, muscle wasting and severe generalized weakness. This resulted in respiratory failure, feeding difficulty, and the ultimate fatality. These pathological findings and clinical regression are closely resembling those seen in human *LAMA2*-CMD (*Zambon et al., 2020; Tan D et al., 2021; Sarkozy et al., 2020; Jain et al., 2019*).

Interestingly, we identified a group of differentially expressed genes (DEGs) related to muscle cytoskeleton development that reached the peak differential expression at P14, coincide with the time when most extensive muscle dystrophic changes were observed in our dy^H/dy^H mice. These observations have also been reported where quantitative proteomic analysis showed that muscle cytoskeleton proteins such as myosin-4, titin, actin, myosin-1, myosin-3 and myosin-8 were dysregulated in dy^{3k}/dy^{3k} mice (*de Oliveira et al., 2014*). Muscle cytoskeleton network was essential for the processes of muscle contraction, force transmission, adaptation of cell shape, cell division and adhesion. For example, F-actin and microtubules regulated cellular elasticity and mechanical contraction, MYHCs provide chemical energy by hydrolysis of ATP, and desmin was associated with the mechanical integrity and mitochondria positioning. Therefore, the dysfunction of cytoskeleton network, especially the decreased F-actin, secondary to laminin α2 deficiency would impair the muscle structure and contractile function in dy^H/dy^H mice, resulting in degeneration and necrosis of muscle fibers.

In addition to the degeneration and necrosis of muscle fibers in dy^H/dy^H mice, we also observed active fiber regenerations. In previous reports, muscle development-related genes such as *MyoD*, *Myh3* and *Myof5* were upregulated in *LAMA2*-CMD mouse models (*Mehuron et al., 2014; Onofre-Oliveira et al., 2012*). Consistent

with the previous reports, the proliferation and differentiation-related genes such as *Myog*, *Myof*, *Myh3* and *Myh8* were upregulated in our current study. Moreover, MYOG, MYOD1 and MYF5 were increased in discrete areas of P14 dy^H/dy^H muscles but the overall levels of MYOG and MYOD1 were decreased by Western blot. These findings indicated that the regeneration of muscle fibers and impaired regeneration occurred simultaneously. However, the mechanisms by which laminin α2 deficiency regulated the expression of these genes requires further investigation.

The laminin α2 chain combines with laminin β1 and γ1 chains to form Lm-211 in the extracellular matrix to form basement membrane and connect with the cell membrane. The extracellular matrix of muscles provides cell microenvironment to maintain the stability of muscle fibers, regulate the transmission of mechanical force, and the development and regeneration of muscle fibers (*Zhang et al., 2021*). As expected, following laminin α2 deficiency in the extracellular matrix, extracellular matrix proteins such as collagen VI and laminin α1, and related genes such as *Col1a2*, *Col5a2*, *Col3a1*, *Tnc*, *Fn1* and *Ctss* were upregulated in dy^H/dy^H mice. Increased expression of extracellular matrix proteins such as Col1a1, Col6α2, collagen III, fibronectin, periostin, galectin-1 and biglycan have been previously reported in *LAMA2*-CMD mouse models (*Mehuron et al., 2014; Gawlik et al., 2019; de Oliveira et al., 2014*). This compensatory hyperplasia of the extracellular matrix resulted in the pathologic fibrosis. Targeted regulation of specific components of extracellular matrix may provide effective treatment strategies (*Ahmad, 2021*).

In summary, the present study provided a novel mouse model dy^H/dy^H for human *LAMA2*-CMD. This was achieved by targeted deletion of exons 3, a common mutation region seen in *LAMA2*-CMD patients. We performed detailed analyses in motor function, muscle and brain pathologies, and detected molecular pathogenetic expressions in these mice and concluded that this is a highly genuine mouse model simulating human disease process. This is the first reported genuine mouse model simulating human *LAMA2*-related muscular dystrophy. This mouse model provides a valuable tool for further investigation into the underlying pathogenesis of human *LAMA2*-CMD and serves as a valid disease model for developing effective therapeutic strategies.

Materials and Methods

Generation of a novel dy^H/dy^H knockout mouse with ΔExon 3 at *Lama2* locus

All studies conducted on the mice were approved by the Animal Ethics Committee of Peking University First Hospital (J202027). All mice were housed and handled according to the guidelines of the Care and Use of Laboratory Animals (NIH Publication, 8th Edition, 2011; http://grants.nih.gov/grants/olaw/Guide-for-the-care-

and-use-of-laboratory-animals.pdf). C57BL/6 mice were used and maintained on a congenic background.

To target the exon 3 of the *Lama2* gene (gene ID 16773), a pair of sgRNAs (5'-ggctgtgtatcactaattccagg-3′, 5'-atggatcaagatcctatagaagg-3′) targeting intron 2 and intron 3 of the *Lama2* gene were designed (**Figure 1A**). The pCS-4G vectors containing sgRNAs and Cas9 mRNA were coinjected into 270 C57BL/6 zygotes which were subsequently implanted into pseudopregnant mice, and 33 pups were born. Nine (3♀, 6♂) of them were genetically identified as heterozygote with a heterozygous 1,625-base pair (bp) deletion at genomic DNA level, and one was selected as F0 founder which was backcrossed with C57BL/6 mice to produce generation F1 mice. F2 mice generated from the crossed heterozygous F1 mice were genetically identified and used for following studies. The genotypes were identified by two polymerase chain reaction (PCR)- amplifications with primers (**Figure 1A**) and PCR products DNA sequencing. The PCR–amplification conditions were as follows: 95 ℃ for 3 min, followed by 30 cycles at 95 ℃ for 15 s, annealing at 62 ℃ for 20 s and elongation at 72 ℃ for 2 min, and a final step at 72 ℃ for 7 min.

The expected sizes observed by 2% agarose electrophoresis analysis were a 1999-bp fragment for the wild-type allele and a 374-bp fragment for the mutant-type allele in the first PCR– amplification, and a 571-bp fragment for the wild-type allele and no fragment for the mutant-type allele in the second PCR- amplification. The F2 mice showing PCR products with a 1999-bp fragment in PCR1 along with a 571-bp fragment in PCR2 were wild-type (WT). Those having a 1999-bp fragment and a 374-bp fragment in PCR1 along with a 571-bp fragment in PCR2 were $dy^H/+$ (Het). Those having a 374-bp fragment in PCR1 along with no fragment in PCR2 were homozygote knockout (KO), dy^H/dy^H mice (**Figure 1B**).

Then, genotype identification was further analyzed by reverse transcription (RT)–PCR. Total RNA was isolated from biceps femoris of WT and dy^H/dy^H, and was reverse transcribed to first strand cDNA using the Reverse Transcription System (A3500, Promega, Madison, Wisconsin, USA). RT–PCR with the forward primer (5'-TGCTTCGAATGCACTCATCACAAC-3′) and the reverse primer (5'-GATATTGTAGAGGGTCAGGCACTCC-3′) was performed to amplify *LAMA2* cDNA exons 2-4. The RT–PCR amplification conditions were as follows: 95 ℃ for 5 min, followed by 35 cycles at 95 ℃ for 30 s, annealing at 56 ℃ for 20 s and elongation at 72 ℃ for 50 s, and a final step at 72 ℃ for 5 min. The RT–PCR products were analyzed by DNA sequencing, and the deletion of exon 3, which resulted in a frameshift downstream sequence of *Lama2* gene, was confirmed at cDNA level in dy^H/dy^H mice (**Figure 1C**).

Single cell RNA sequencing and data process

Two total brains were extracted from 21 days of age dy^H/dy^H and WT mouse. Single cell RNA-seq libraries

were constructed using the Chromium Single Cell 3' Reagent Kit (10 x Genomics) according to the manufacturer's protocol on the brain tissue. Sequencing was performed on Illumina platform. The raw data were processed by CellRanger (https://support.10xgenomics.com/single-cell-gene-expression/software/pipelines/latest/what-is-cell-ranger) to perform sample demultiplexing, barcode processing and single cell 3′ gene counting. The cDNA reads were aligned to the mm10 premRNA reference genome. Only confidently mapped reads with valid barcodes and unique molecular identifiers were used to generate the gene-barcode matrix. Further analyses for quality filtering were performed using the Seurat V4.3 R package. Cells, which have unique feature counts over 3,000 or less than 200 or have > 5% mitochondrial counts, were filtered. After quality filtering and removing unwanted cells from the dataset, we normalized the data by the total expression, multiplied by a scale factor of 10,000 and log-transformed the result, then we performed Cell clustering, gene expression visualization, marker genes identification and differential expression analysis. The threshold for differential expressed genes was set as |log2FoldChange| > 0.5 and p value < 0.05. Then clusterProfiler V4.8 was used for GO and KEGG enrichment of the differentially expressed genes. CellChat V1.6 was used to analyze the cell-cell communications between cell clusters and compared the difference of cell-cell communications between dy^H/dy^H and WT.

RNA isolation and RNA sequencing

The biceps femoris was obtained from 14-day-old mice of WT (n = 4), Het (n = 6) and dy^H/dy^H (KO) (n = 6). Total RNA was isolated from the biceps femoris using TRIzol (Invitrogen, Carlsbad, CA). The RNA samples were submitted to CapitalBio (https://www.capitalbiotech.com) for next-generation sequencing with the TruSeq RNA Exome. Paired-end sequencing (2 × 150 bp reads) was performed on successful RNA libraries using the Illumina HiSeq X-Ten platform. During the experiment, investigators were blinded to the samples' information. The quality of raw reads was first assessed using FastQC. After filtering out low-quality bases and adaptors using FastP, reads were mapped to the mouse genome assembly GRCh38 (Mus_musculus.GRCm38.dna.toplevel.REF.fa) using Hisat2. Samples were subjected to quality control by examining the percentage of reads uniquely mapping to the genome, the percentage of reads mapping to known protein coding sequences, and the number of genes with 90% base coverage. Gene fusions were identified by mapping reads to the mouse genome using StringTie. The additional information about the hidden correlations within obtained dataset was extracted by principal component analysis using dimension reduction which reduces the dimensionality of the original data matrix retaining the maximum amount of variability. Differentially

expressed genes (DEGs) were identified by counting the number of reads mapping to each gene from Ensemble 96 (ftp://ftp.ensembl.org/pub/release-96/fasta/mus_musculus/dna/Mus_musculus.GRCm38.dna.toplevel.fa.gz) using featureCounts and StringTie. Transcripts per million (TPM) were analyzed using Stringtie software. The R package DESeq2 was used to detect DEGs and normalize the read count. The Pearson correlation of each sample showed that all samples were highly correlated. The R package clusterProfiler was used for GO function (http://www.geneontology.org/) and GSEA KEGG analysis. Additionally, Gene Set Variation Analysis (GSVA) was employed for GO function and KEGG pathway analysis using the R package GSVA, and the limma package (version 3.25.15; bioinf.wehi.edu.au/limma) was used to detect the differentially enriched functions and pathways (|log2FC|>=1, p-value < 0.05). A clustering dendrogram was used to display the results of dynamic tree cutting and merging.

Muscle pathology, immunofluorescence, and immunohistochemistry

Skeletal muscles (biceps femoris, quadriceps femoris and triceps brachii) were isolated from WT and dy^H/dy^H mice at P1, P4, P7, P14 and P21. Gastrocnemius muscle, diaphragm, heart, tongue and intestinal muscles were isolated from WT and dy^H/dy^H mice at P14. Muscle tissues were embedded in optimal cutting temperature compound (Tissue Tek, Torrance, CA) and frozen in liquid nitrogen. Seven μm thick transverse cryosections were stained with hematoxylin and eosin (H&E, Solarbio, Beijing, China), and Sirius Red or subjected to immunostaining. Immunofluorescence was performed according to standard procedures with antibodies against the N-terminus of the laminin α2 chain (rat monoclonal, 4H8-2, Sigma, Saint Louis, USA), the laminin α1 chain (rat monoclonal, MAB4656, R&D Systems, Minneapolis, USA), myogenic differentiation antigen 1 (MYOD1) (mouse monoclonal, ab16148, Abcam, Cambridge, UK), myogenin (MYOG) (mouse monoclonal, MAB66861, R&D Systems, Minneapolis, USA), myogenic factor 5 (MYF5) (mouse monoclonal, MAB4027, R&D Systems, Minneapolis, USA), myosin heavy chain (MYHC) (mouse monoclonal, MAB4470, R&D Systems, Minneapolis, USA), desmin (mouse monoclonal, MA5-15306, invitrogen, CA) and CD68 (rabbit IgG, BA3638, Boster, CA) . The secondary antibodies were goat anti-rat IgG 488, goat anti- mouse IgG 488/594, and goat anti-rabbit IgG 488/594 (Abcam, Cambridge, UK).

The slides for H&E, Sirius Red and immunohistochemistry staining were observed by Leica microscopy (DFC295, Wetzlar, Germany) with LAS V4.12, and the slides for immunofluorescence were imaged by a confocal microscope with FV3000 system (Olympus FluoView FV10i, Tokyo, Japan).

Western blot analysis

Total protein was extracted from mouse muscle tissues using RIPA solution (Pplygen, Beijing, China). The protein concentration was determined by a BCA protein assay (Thermo Fisher Scientific Inc., Waltham, MA). Then, denatured proteins were separated by sodium dodecyl sulfate polyacrylamide gels (SDS–PAGE) and transferred to a polyvinylidene fluoride membrane. Electrochemiluminescence was used to observe the bands with an imaging system (molecular imager, ChemiDoc XRS, Bio–Rad, CA). The densities of the bands were determined semiquantitatively by ImageJ software (NIH, Bethesda, MD). Equal protein loading of blots was confirmed by immunoblotting of GAPDH (rabbit monoclonal, #2118, Cell Signaling Technology, Danvers, USA), except β-tubulin (mouse monoclonal, 86298, Cell Signaling Technology, Danvers, USA) used as equal protein for laminin α2. The results were represented as fold of change over the control (wild-type group) value. The antibodies used in this study were as follows: laminin α2 chain (rat monoclonal, 4H8-2, Sigma, Saint Louis, USA), MYOD1 (mouse monoclonal, ab64159, Abcam, Cambridge, UK), MYOG (mouse monoclonal, MAB66861, R&D Systems, Minneapolis, USA), myosin heavy chain 2 (MYH2) (rabbit monoclonal, ab124937, Abcam, Cambridge, UK), MYHC (mouse monoclonal, MAB4470, R&D Systems, Minneapolis, USA), desmin (mouse monoclonal, MA5-15306, Invitrogen, CA), α-actin (rabbit polyclonal, 23660-I-AP, Proteintech, Rosemont, USA), F-actin (rabbit polyclonal, bs-1571R, Bioss, Rosemont, USA). Then, the blots were incubated with horseradish peroxidase-conjugated secondary antibodies (Cell Signaling Technology, Danvers, USA).

Four limbs grip strength test

Muscle strength measurements of the four limbs of mice were performed from P10-P24 using a grip strength meter and SuperGSM software (Shanghai XinRuan Information Technology Co., Ltd.). All four paws of each mouse were allowed to grasp the grid attached to the grip strength meter. After obtaining a good grip, the mouse was pulled away from the grid until the grasp broke. The test was repeated 3 times for each mouse and the mean value was calculated. The results are presented as normalized strength (gram force per gram body weight) (*Elbaz et al., 2012*). Four-limb grip strength was measured by one person for all trials due to the outcome possibly being highly variable between experimenters.

Treadmill exercise protocol

The mice were forced to run on a motorized treadmill for training prior to the experiment once a day from P13 to P17. The experiment was performed beginning on P18. The dy^H/dy^H mice that were too fatigued to run were removed from the experiment. The exercise load consisted of 5 min break and interval running cycles for 25 min at a speed of 1 meter/min for 20 s and 2 meters/min for 20 s, with a 0° inclination. Motivation to run was induced by applying 1.0 mA electric foot shocks, one set of electric foot shocks with a 10 s duration. The gait

and number of electric shocks were observed.

Determination of the serum CK levels

Approximately 200 μL of blood from each mouse was collected, centrifuged at 4000 rpm for 10 min at 4 °C, and analyzed for CK levels using a mouse CK ELISA Kit (Nanjing Herb-Source Bio-Technology CO., LTD, czy24506). To determine the CK levels, the serum samples were diluted stepwise, 5-, 20-, and 50-fold because the CK level was beyond the linear range, and the CK level was then measured and recorded at the highest dilution.

Muscle MR acquisition

Siemens TIM Trio 3.0 T MRI scanner (Siemens, Erlangen, Germany) was used to detect changes in the muscles. The mice were anesthetized by intraperitoneal injection of 5% chloral hydrate (7 mL/kg), and then placed prostrate on a holder bed with the hip and hindlimbs moved into the center of a small animal-specific coil. High resolution T1-weighted and T2-weighted MRI of the hip and hindlimb muscles were acquired under optimized imaging parameters. Relative muscle area (muscle area/fat area) was quantified on T1-weighted MRI, and heterogeneity was quantified in muscles on T2-weighted MRI by averaging the mean intensities in 8-11 regions of interest (ROIs) in 3 slices using ImageJ software (NIH, Bethesda, MD) (*Iyer et al., 2020*). Images were converted to Digital Imaging and Communication in Medicine (DICOM) format using syngo MR B17 software (Siemens, Erlangen, Germany).

Statistical analysis

An unpaired t-test was used to compare the mean between groups. All graphs related to phenotype analysis were generated using GraphPad Prism 8 software (GraphPad Software, La Jolla, CA). Graphs displayed the mean ± standard deviation (SD). All graphs related to RNA sequencing analysis of mouse muscle tissues were performed using R software version 4.0.4. Statistical analyses were performed using SPSS (version 19.0; IBM-SPSS, Chicago, IL). Two-sided $p < 0.05$ was considered to be statistically significant.

References

1. Abdel Aleem A, Elsaid MF, Chalhoub N, Chakroun A, Mohamed KAS, AlShami R, Kuzu O, Mohamed RB, Ibrahim K, AlMudheki N, Osman O, Ross ME, ELalamy O. 2020. Clinical and genomic characteristics of *LAMA2* related congenital muscular dystrophy in a patients' cohort from Qatar. A population specific founder variant. *Neuromuscul Disord* 30:457-471. DOI: https://doi.org/10.1016/j.nmd.2020.03.009. PMID: 32444167
2. Ahmad V. 2021. Prospective of extracellular matrix and drug correlations in disease management. *Asian J Pharm Sci* 16:147-160. DOI: https://doi.org/10.1016/j.ajps.2020.06.007. PMID: 33995610
3. Arreguin AJ, Colognato H. 2020. Brain Dysfunction in LAMA2-Related Congenital Muscular Dystrophy: Lessons From Human Case Reports and Mouse Models. *Front Mol Neurosci* 13:118. DOI: https://doi.org/10.3389/fnmol.2020.00118. PMID: 32792907
4. Aumailley M. 2021. Laminins and interaction partners in the architecture of the basement membrane at the dermal-epidermal junction. *Exp Dermatol* 30:17-24. DOI: https://doi.org/10.1111/exd.14239. PMID: 33205478
5. Barazesh M, Mohammadi S, Bahrami Y, Mokarram P, Morowvat MH, Saidijam M, Karimipoor M, Kavousipour S, Vosoughi AR, Khanaki K. 2021. CRISPR/Cas9 Technology as a Modern Genetic Manipulation Tool for Recapitulating of Neurodegenerative Disorders in Large Animal Models. Curr Gene Ther 21:130-148. DOI: https://doi.org/10.2174/1566523220666201214115024. PMID: 33319680
6. Barkovich AJ, Dobyns WB, Guerrini R. 2015. Malformations of cortical development and epilepsy. *Cold Spring Harb Perspect Med* 5:a022392. DOI: https://doi.org/10.1101/cshperspect.a022392. PMID: 25934463
7. Devisme L, Bouchet C, Gonzalès M, Alanio E, Bazin A, Bessières B, Bigi N, Blanchet P, Bonneau D, Bonnières M, Bucourt M, Carles D, Clarisse B, Delahaye S, Fallet-Bianco C, Figarella-Branger D, Gaillard D, Gasser B, Delezoide AL, Guimiot F, Joubert M, Laurent N, Laquerrière A, Liprandi A, Loget P, Marcorelles P, Martinovic J, Menez F, Patrier S, Pelluard F, Perez MJ, Rouleau C, Triau S, Attié-Bitach T, Vuillaumier-Barrot S, Seta N, Encha-Razavi F. 2012. Cobblestone lissencephaly: neuropathological subtypes and correlations with genes of dystroglycanopathies. *Brain* 135:469-482. DOI: https://doi.org/10.1093/brain/awr357. PMID: 22323514
8. Decostre V, Vignaud A, Matot B, Huguet A, Ledoux I, Bertil E, Gjata B, Carlier PG, Gourdon G, Hogrel JY. 2013. Longitudinal in vivo muscle function analysis of the DMSXL mouse model of myotonic

dystrophy type 1. *Neuromuscular Disorders* 23:1016-1025. DOI: https://doi.org/10.1016/j.nmd.2013.07.014. PMID: 24139022

9. de Oliveira BM, Matsumura CY, Fontes-Oliveira CC, Gawlik KI, Acosta H, Wernhoff P, Durbeej M. 2014. Quantitative proteomic analysis reveals metabolic alterations, calcium dysregulation, and increased expression of extracellular matrix proteins in laminin alpha2 chain-deficient muscle. *Mol Cell Proteomics* 13:3001-3013. DOI: https://doi.org/10.1074/mcp.M113.032276. PMID: 24994560
10. Durbeej M. 2015. Laminin-alpha2 Chain-Deficient Congenital Muscular Dystrophy: Pathophysiology and Development of Treatment. *Curr Top Membr* 76:31-60. DOI: https://doi.org/10.1016/bs.ctm.2015.05.002. PMID: 26610911
11. Durbeej M. 2010. Laminins. *Cell Tissue Res* 339:259-268. DOI: https://doi.org/10.1007/s00441-009-0838-2. PMID: 19693542
12. Elbaz M, Yanay N, Aga-Mizrachi S, Brunschwig Z, Kassis I, Ettinger K, Barak V, Nevo Y. 2012. Losartan, a therapeutic candidate in congenital muscular dystrophy: Studies in the dy2J/dy2J Mouse. *Annals of Neurology* 71:699-708. DOI: https://doi.org/10.1002/ana.22694. PMID: 22522482
13. Gawlik KI, Durbeej MA. 2020. Family of Laminin alpha2 Chain-Deficient Mouse Mutants: Advancing the Research on *LAMA2*-CMD. *Front Mol Neurosci* 13:59. DOI: https://doi.org/10.3389/fnmol.2020.00059. PMID: 32457577
14. Gawlik KI, Holmberg J, Svensson M, Einerborg M, Oliveira BM, Deierborg T, Durbeej M. 2017. Potent pro-inflammatory and pro-fibrotic molecules, osteopontin and galectin-3, are not major disease modulators of laminin alpha2 chain-deficient muscular dystrophy. *Sci Rep* 7:44059. DOI: https://doi.org/10.1038/srep44059. PMID: 28281577
15. Gawlik KI, Körner Z, Oliveira BM, Durbeej M. 2019. Early skeletal muscle pathology and disease progress in the dy(3K)/dy(3K) mouse model of congenital muscular dystrophy with laminin alpha2 chain-deficiency. *Sci Rep* 9:14324. DOI: https://doi.org/10.1038/s41598-019-50550-0.PMID: 31586140
16. Ge L, Zhang C, Wang Z, Chan SHS, Zhu W, Han C, Zhang X, Zheng H, Wu L, Jin B, Shan J, Mao B, Zhong J, Peng X, Cheng Y, Hu J, Sun Y, Lu J, Hua Y, Zhu S, Wei C, Wang S, Jiao H, Yang H, Fu X, Fan Y, Chang X, Wang S, Bao X, Zhang Y, Wang J, Wu Y, Jiang Y, Yuan Y, Rutkowski A, Bönnemann CG, Wei W, Wu X, Xiong H. 2019. Congenital muscular dystrophies in China. *Clin Genet* 96:207-215. DOI: https://doi.org/10.1111/cge.13560. PMID: 31066047

17. Ge L, Liu A, Gao K, Du R, Ding J, Mao B, Hua Y, Zhang X, Tan D, Yang H, Fu X, Fan Y, Zhang L, Song S, Wu J, Zhang F, Jiang Y, Wu X, Xiong H. 2018. Deletion of exon 4 in LAMA2 is the most frequent mutation in Chinese patients with laminin alpha2-related muscular dystrophy. *Sci Rep* 8:14989. DOI: https://doi.org/10.1038/s41598-018-33098-3. PMID: 30301903
18. Hagg T, Portera-Cailliau C, Jucker M, Engvall E. 1997. Laminins of the adult mammalian CNS; laminin-alpha2 (merosin M-) chain immunoreactivity is associated with neuronal processes. *Brain Res* 764:17-27. DOI: https://doi.org/10.1016/s0006-8993(97)00419-8. PMID: 9295189
19. Hohenester E. 2019. Laminin G-like domains: dystroglycan-specific lectins. *Curr Opin Struct Biol* 56:56-63. DOI: https://doi.org/10.1016/j.sbi.2018.11.007. PMID: 30530204
20. Huang T, Wang K, Li Y, Ye Y, Chen Y, Wang J, Yao C. 2022. Construction of a Novel Ferroptosis-Related Gene Signature of Atherosclerosis. *Front Cell Dev Biol* 9:800833. DOI: https://doi.org/10.3389/fcell.2021.800833. PMID: 35071238
21. Huang X, Tan D, Zhang Z, Ge L, Liu J, Ding J, Yang H, Wei C, Chang X, Yuan Y, Yan C, Xiong H. 2023. Unique Genotype-Phenotype Correlations within *LAMA2*-related Limb Girdle Muscular Dystrophy in Chinese Patients. *Front Neurol* 14:1158094. DOI: https://doi.org/10.3389/fneur.2023.1158094. PMID: 37206914
22. Iyer SR, Xu S, Shah SB, Lovering RM. 2020. Muscle phenotype of a rat model of Duchenne muscular dystrophy. *Muscle Nerve* 62:757-761. DOI: https://doi.org/10.1002/mus.27061. PMID: 32918339
23. Jain MS, Meilleur K, Kim E, Norato G, Waite M, Nelson L, McGuire M, Duong T, Keller K, Lott DJ, Glanzman A, Rose K, Main M, Fiorini C, Chrismer I, Linton M, Punjabi M, Elliott J, Tounkara F, Vasavada R, Logaraj R, Winkert J, Donkervoort S, Leach M, Dastgir J, Hynan L, Nichols C, Hartnett E, Averion GM, Collins JC, Kim ES, Kokkinis A, Schindler A, Zukosky K, Fee R, Hinton V, Mohassel P, Bharucha-Goebel D, Vuillerot C, McGraw P, Barton M, Fontana J, Rutkowski A, Foley AR, Bönnemann CG. 2019. Longitudinal changes in clinical outcome measures in COL6-related dystrophies and *LAMA2*-related dystrophies. *Neurology* 93:e1932-e1943. DOI: https://doi.org/10.1212/WNL.0000000000008517. PMID: 31653707
24. Jin S, Guerrero-Juarez CF, Zhang L, Chang I, Ramos R, Kuan CH, Myung P, Plikus MV, Nie Q. 2021. Inference and analysis of cell-cell communication using CellChat. *Nat Commun* 12:1088. DOI: https://doi.org/10.1038/s41467-021-21246-9. PMID: 33597522

25. Jayakody H, Zarei S, Nguyen H, Dalton J, Chen K, Hudgins L, Day J, Withrow K, Pandya A, Teasley J, Dobyns WB, Mathews KD, Moore SA. 2020. Cobblestone Malformation in LAMA2 Congenital Muscular Dystrophy (MDC1A). *J Neuropathol Exp Neurol* 79:998-1010. DOI: https://doi.org/10.1093/jnen/nlaa062. PMID: 32827036
26. Mehuron T, Kumar A, Duarte L, Yamauchi J, Accorsi A, Girgenrath M. 2014. Dysregulation of matricellular proteins is an early signature of pathology in laminin-deficient muscular dystrophy. *Skeletal Muscle* 4:14. DOI: https://doi.org/10.1186/2044-5040-4-14. PMID: 25075272
27. Menezes MJ, McClenahan FK, Leiton CV, Aranmolate A, Shan X, Colognato H. 2014. The extracellular matrix protein laminin alpha2 regulates the maturation and function of the blood-brain barrier. *J Neurosci* 34:15260-15280. DOI: https://doi.org/10.1523/JNEUROSCI.3678-13.2014. PMID: 25392494
28. Mohassel P, Foley AR, Bonnemann CG. 2018. Extracellular matrix-driven congenital muscular dystrophies. *Matrix Biol* 71-72:188-204. DOI: https://doi.org/10.1016/j.matbio.2018.06.005. PMID: 29933045
29. Nguyen Q, Lim KRQ, Yokota T. 2019. Current understanding and treatment of cardiac and skeletal muscle pathology in laminin-alpha2 chain-deficient congenital muscular dystrophy. *Appl Clin Genet* 12:113-130. DOI: https://doi.org/10.2147/TACG.S187481. PMID: 31308722
30. Onofre-Oliveira PC, Santos AL, Martins PM, Ayub-Guerrieri D, Vainzof M. 2012. Differential expression of genes involved in the degeneration and regeneration pathways in mouse models for muscular dystrophies. *Neuromolecular Med* 14:74-83. DOI: https://doi.org/10.1007/s12017-012-8172-3. PMID: 22362587
31. Porcari P, Hall MG, Clark CA, Greally E, Straub V, Blamire AM. 2020. Time-dependent diffusion MRI as a probe of microstructural changes in a mouse model of Duchenne muscular dystrophy. *Nmr Biomed* 33:e4276. DOI: https://doi.org/10.1002/nbm.4276. PMID: 32101354
32. Sarkozy A, Foley AR, Zambon AA, Bönnemann CG, Muntoni F. 2020. *LAMA2*-Related Dystrophies: Clinical Phenotypes, Disease Biomarkers, and Clinical Trial Readiness. *Front Mol Neurosci* 13:123. DOI: https://doi.org/10.3389/fnmol.2020.00123. PMID: 32848593
33. Severino M, Geraldo AF, Utz N, Tortora D, Pogledic I, Klonowski W, Triulzi F, Arrigoni F, Mankad K, Leventer RJ, Mancini GMS, Barkovich JA, Lequin MH, Rossi A. 2020. Definitions and classification of malformations of cortical development: practical guidelines. *Brain* 143:2874-2894. DOI: https://doi.org/10.1093/brain/awaa174. PMID: 32779696

34. Sframeli M, Sarkozy A, Bertoli M, Astrea G, Hudson J, Scoto M, Mein R, Yau M, Phadke R, Feng L, Sewry C, Fen ANS, Longman C, McCullagh G, Straub V, Robb S, Manzur A, Bushby K, Muntoni F. 2017. Congenital muscular dystrophies in the UK population: Clinical and molecular spectrum of a large cohort diagnosed over a 12-year period. *Neuromuscul Disord* 27:793-803. DOI: https://doi.org/10.1016/j.nmd.2017.06.008. PMID: 28688748
35. Sztretye M, Szabó L, Dobrosi N, Fodor J, Szentesi P, Almássy J, Magyar ZÉ, Dienes B, Csernoch L. 2020. From Mice to Humans: An Overview of the Potentials and Limitations of Current Transgenic Mouse Models of Major Muscular Dystrophies and Congenital Myopathies. *Int J Mol Sci* 21:8935. DOI: https://doi.org/10.3390/ijms21238935. PMID: 33255644
36. Tan D, Ge L, Fan Y, Chang X, Wang S, Wei C, Ding J, Liu A, Wang S, Li X, Gao K, Yang H, Que C, Huang Z, Li C, Zhu Y, Mao B, Jin B, Hua Y, Zhang X, Zhang B, Zhu W, Zhang C, Wang Y, Yuan Y, Jiang Y, Rutkowski A, Bönnemann CG, Wu X, Xiong H. 2021. Natural history and genetic study of *LAMA2*-related muscular dystrophy in a large Chinese cohort. *Orphanet J Rare Dis* 16:319. DOI: https://doi.org/10.1186/s13023-021-01950-x. PMID: 34281576
37. van Putten M, Lloyd EM, de Greef JC, Raz V, Willmann R, Grounds MD. 2020. Mouse models for muscular dystrophies: an overview. *Dis Model Mech* 13:dmm043562. DOI: https://doi.org/10.1242/dmm.043562. PMID: 32224495
38. Villanova M, Malandrini A, Sabatelli P, Sewry CA, Toti P, Torelli S, Six J, Scarfó G, Palma L, Muntoni F, Squarzoni S, Tosi P, Maraldi NM, Guazzi GC. 1997. Localization of laminin alpha 2 chain in normal human central nervous system: an immunofluorescence and ultrastructural study. *Acta Neuropathol* 94:567-571. DOI: https://doi.org/10.1007/s004010050751. PMID: 9444358
39. Villanova M, Malandrini A, Toti P, Salvestroni R, Six J, Martin JJ, Guazzi GC. 1996. Localization of merosin in the normal human brain: implications for congenital muscular dystrophy with merosin deficiency. *J Submicrosc Cytol Pathol* 28:1-4. PMID: 8929621
40. Vohra R, Accorsi A, Kumar A, Walter G, Girgenrath M. 2015. Magnetic Resonance Imaging Is Sensitive to Pathological Amelioration in a Model for Laminin-Deficient Congenital Muscular Dystrophy (MDC1A). *Plos One* 10:e0138254. DOI: https://doi.org/10.1371/journal.pone.0138254. PMID: 26379183
41. Yurchenco PD, McKee KK, Reinhard JR, Ruegg MA. 2018. Laminin-deficient muscular dystrophy: Molecular pathogenesis and structural repair strategies. *Matrix Biol* 71-72:174-187. DOI: https://doi.org/10.1016/j.matbio.2017.11.009. PMID: 29191403

42. Zambon AA, Ridout D, Main M, Mein R, Phadke R, Muntoni F, Sarkozy A. 2020. *LAMA2*-related muscular dystrophy: Natural history of a large pediatric cohort. *Ann Clin Transl Neurol* 7:1870-1882. DOI: https://doi.org/10.1002/acn3.51172. PMID: 32910545

43. Zhang W, Liu Y, Zhang H. 2021. Extracellular matrix: an important regulator of cell functions and skeletal muscle development. *Cell Biosci* 11:65. DOI: https://doi.org/10.1186/s13578-021-00579-4. PMID: 33789727

Figure legends

Figure 1. Generation of a mouse model with deletion of exon 3 (ΔExon 3) in the *Lama2* gene. (A) Strategy of generation of ΔExon 3 mice (dy^H/dy^H mice) by clustered regularly interspaced short palindromic repeats (CRISPR)-Cas9. The sequences of the *Lama2* gene marked with blue indicated sgRNAs targeting sequences, ones marked with brown indicated the location of polymerase chain reaction (PCR) primers (*Lama2*-F, *Lama2*-R1, and *Lama2*-R2), respectively. **(B)** PCR analysis for genotype identification of the F2 mice. **c,** DNA sequencing of reverse transcription (RT)-PCR products from dy^H/dy^H muscle validated the deletion of exon 3, which resulted in a frameshift downstream sequence of *Lama2* gene.

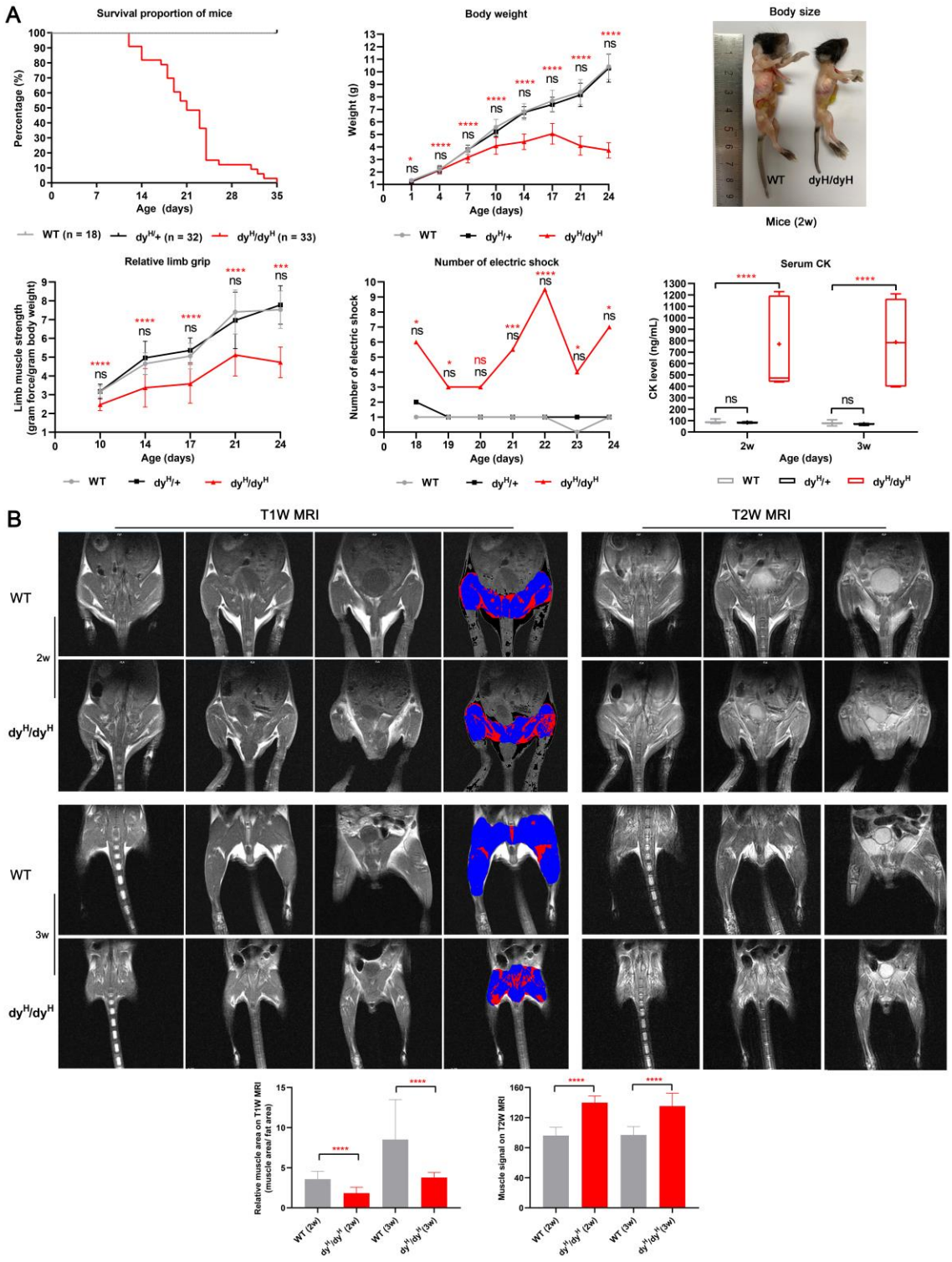

Figure 2. General phenotype and muscle MRI of dy^H/dy^H mice. (A) General phenotype of dy^H/dy^H mice. There was no significant difference in survival, body weight, muscle function (four-limb grip and the number of electric shocks on the treadmill) and serum CK levels between the wild-type (WT) and heterozygous mice at each point. Kaplan–Meier survival analysis revealed that the median survival of dy^H/dy^H mice was 21 days (range 12-35 days), and none of the wild-type and heterozygous mice died during the observation period.

Significant difference in body weight (g) between the WT and dy^H/dy^H mice was marked at P7 (3.74 *vs* 3.16, t-test, $p < 0.001$), P10 (5.58 *vs* 4.09, t-test, $p < 0.001$), P14 (6.81 *vs* 4.41, t-test, $p < 0.001$), P17 (7.66 *vs* 5.04, t-test, $p < 0.001$), P21 (8.34 *vs* 4.09, t-test, $p< 0.001$), and P24 (10.41 *vs* 3.73, t-test, $p < 0.001$). Two-week-old dy^H/dy^H mice could be easily identified due to their smaller size. Significant differences in the mean relative four-limb grip (force per gram body weight) between the WT and dy^H/dy^H mice were marked at P10 (3.16 *vs* 2.46, t-test, $p < 0.001$), P14 (4.65 *vs* 3.37, t-test, $p < 0.001$), P17 (5.05 *vs* 3.58, t-test, $p = 0.001$), P21 (7.41 *vs* 5.12, t-test, $p< 0.001$), and P24 (7.53 *vs* 4.73, t-test, $p = 0.003$). The mean number of electric shocks on the treadmill significantly increased number of the electric shocks in dy^H/dy^H mice at P18 (t-test, $p = 0.010$), P19 (t-test, $p = 0.012$), P21 (t-test, $p = 0.003$), P22 (t-test, $p < 0.001$), P23 (t-test, $p = 0.017$), and P24 (t-test, $p = 0.010$). Approximately 9-10 times higher CK levels were detected in dy^H/dy^H mice than in WT mice at P14 and P21. *$p < 0.05$, **$p < 0.01$, ***$p < 0.005$, ****$p < 0.001$, ns ($p \geq 0.05$), blue 'ns' for wild-type *vs* heterozygous mice, black 'ns' for *vs* dy^H/dy^H mice at two ages, and orange asterisks or 'ns' for WT *vs* dy^H/dy^H mice. **(B)** Muscle MRI in dy^H/dy^H mice. Pelvic and hindlimb muscle MRI showed significantly smaller muscle volumes on T1-weighted MRI and significantly increased hyperintense regions on T2-weighted muscle MRI in dy^H/dy^H mice than in WT mice at P14 and P21 (****$p < 0.001$).

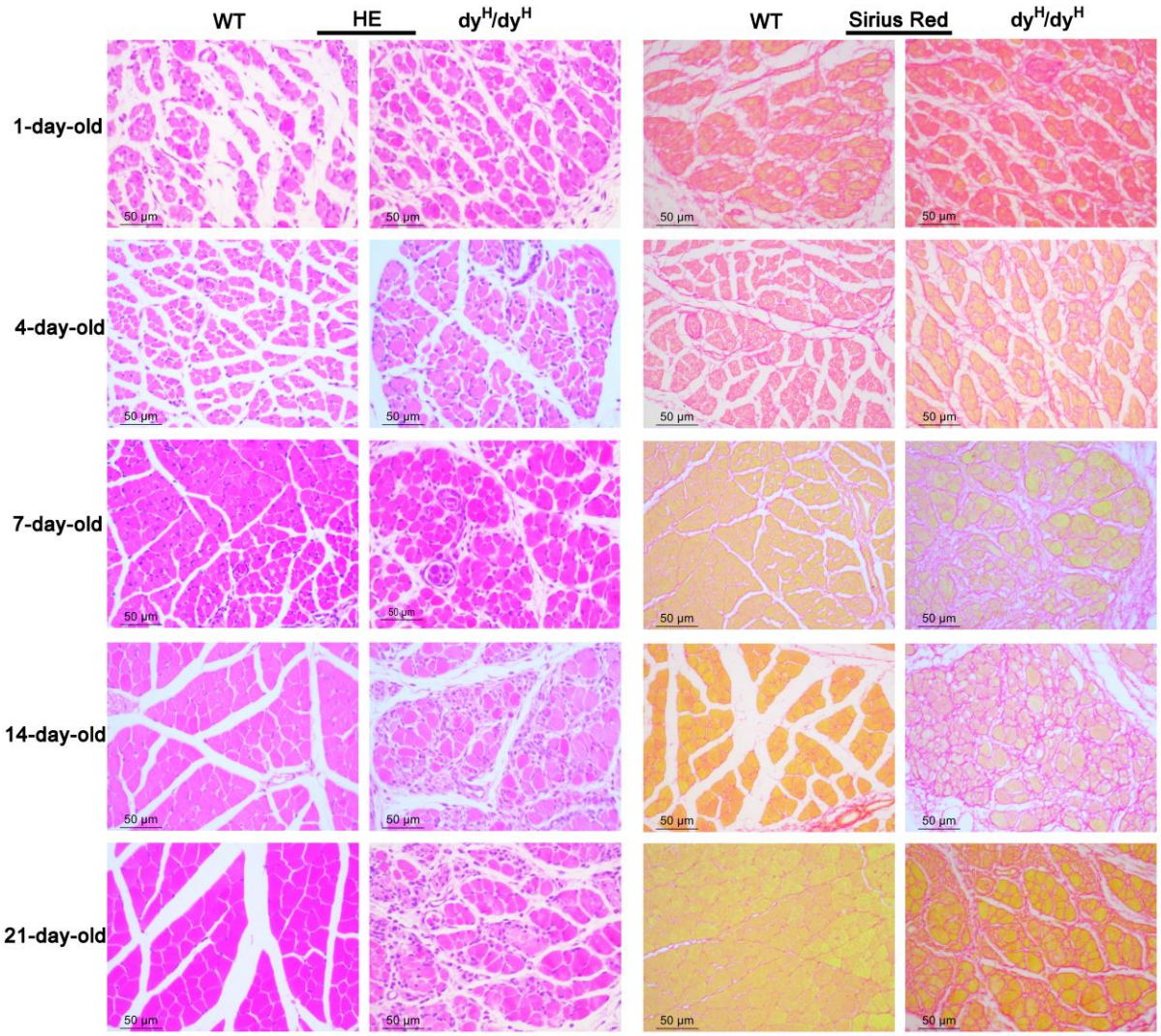

Figure 3. Muscle pathology with age in the biceps femoris of dy^H/dy^H mice. H&E and Sirius Red staining of the biceps femoris were compared between wild-type and dy^H/dy^H mice at P1, P4, P7, P14 and P21. H&E staining showed a noticeable inequality muscle fiber size in P7 dy^H/dy^H mice, the most extreme dystrophic changes (inequality muscle fiber size, degeneration, necrosis and regeneration of muscle fibers), and connective tissue penetration and inflammation in P14 dy^H/dy^H mice. Sirius Red staining showed increased collagen content and fibrosis in dy^H/dy^H mice from P7.

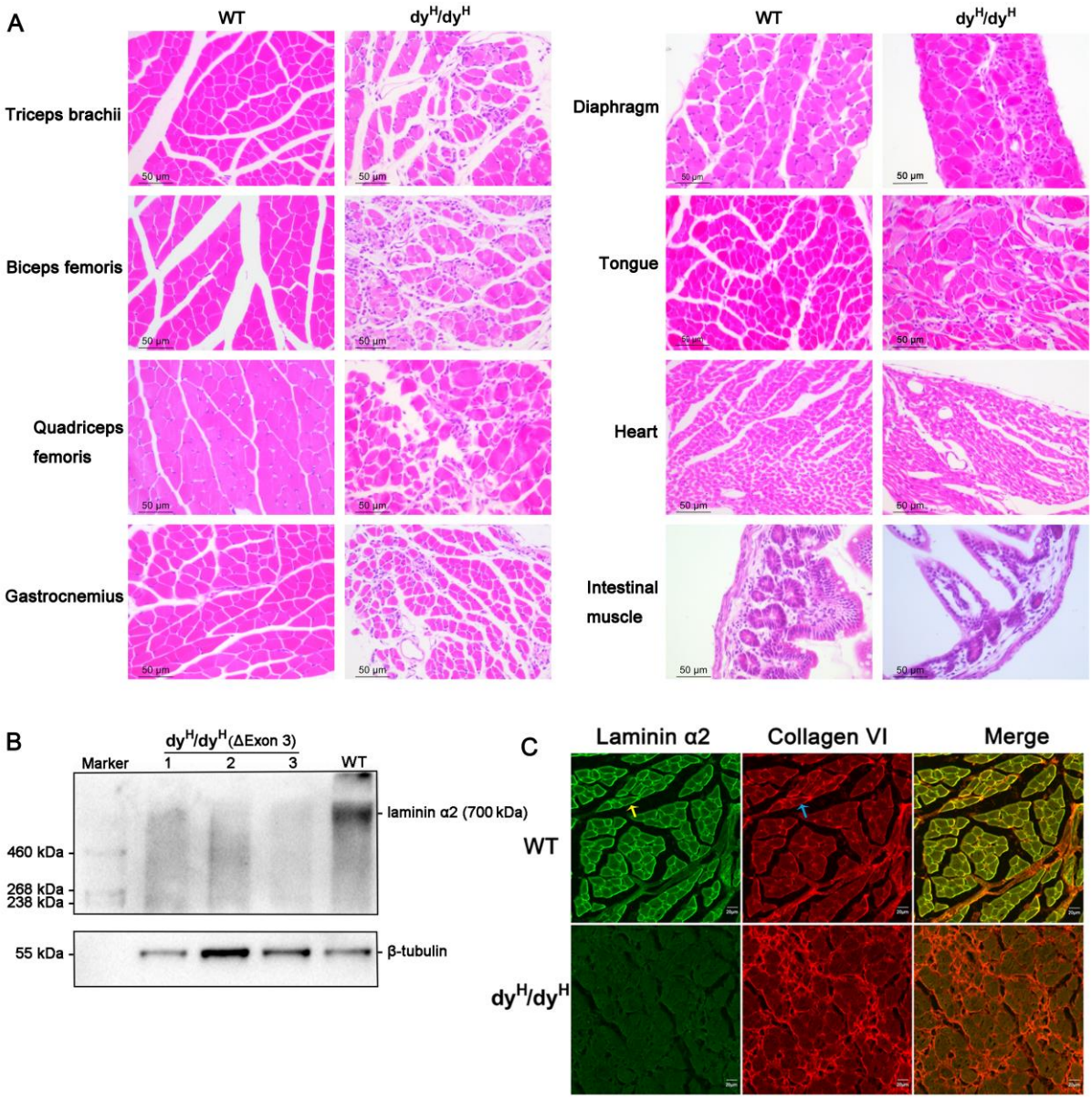

Figure 4. Extensive involvement with muscle pathology and laminin α2 deficiency in dy^H/dy^H mice. (A) H&E staining showed dystrophic changes in the quadriceps femoris, gastrocnemius, triceps brachii, diaphragm and tongue muscles, but not as much as in the biceps femoris, while the heart and intestinal muscles were spared. **(B)** The 300 kDa fragment of laminin α2 chain and 700 kDa laminin-α2β1γ1 (LM-211) complex were not detected in the biceps femoris of dy^H/dy^H mice (n = 3) by Western blot analysis. **(C)** Colocalization of laminin α2 chain (green fluorescence, yellow arrow) and collagen VI (red fluorescence, blue arrow) showed that they were normally located and expressed in the basement membrane in WT muscle, but laminin α2 deficiency along with increased collagen VI were observed in dy^H/dy^H muscle.

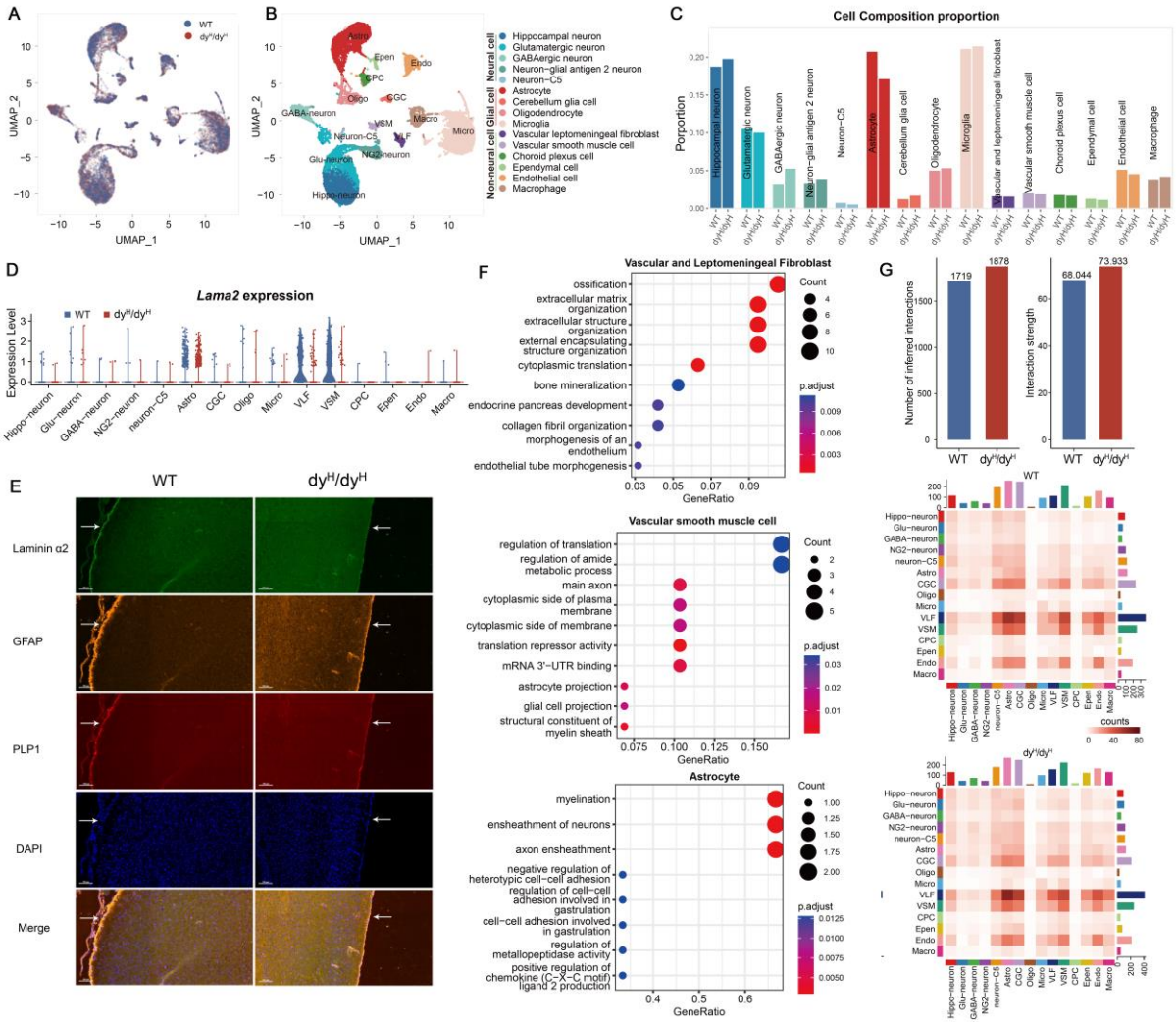

Figure 5. scRNA-seq analysis of brains from dy^{H}/dy^{H} and WT mice. (A) UMAP visualization of all the cells colored by sample. **(B)** UMAP visualization of all the cells from dy^{H}/dy^{H} and WT brains colored by cluster identity. **(C)** Cell composition proportion of every annotated cell cluster in dy^{H}/dy^{H} and WT separately. **(D)** Violin plots of the expression of *Lama2* gene in WT and dy^{H}/dy^{H} in each annotated cell cluster. **(E)** Immunofluorescence of laminin α2, GFAP (astrocytes), and PLP1 on P14 mouse brain slices. DAPI was for nuclei staining. White arrows indicated the cortical surface. **(F)** GO enrichment of differentially expressed genes in vascular and leptomeningeal fibroblasts, vascular smooth muscle cells and astrocytes. **(G)** Cell-cell communications among cell clusters. Total number of inferred cell-cell interaction counts (left) and strength (right) in dy^{H}/dy^{H} and WT, respectively. Heatmap of ligand-receptor interaction counts in all pairwise cell clusters in WT and dy^{H}/dy^{H} brains.

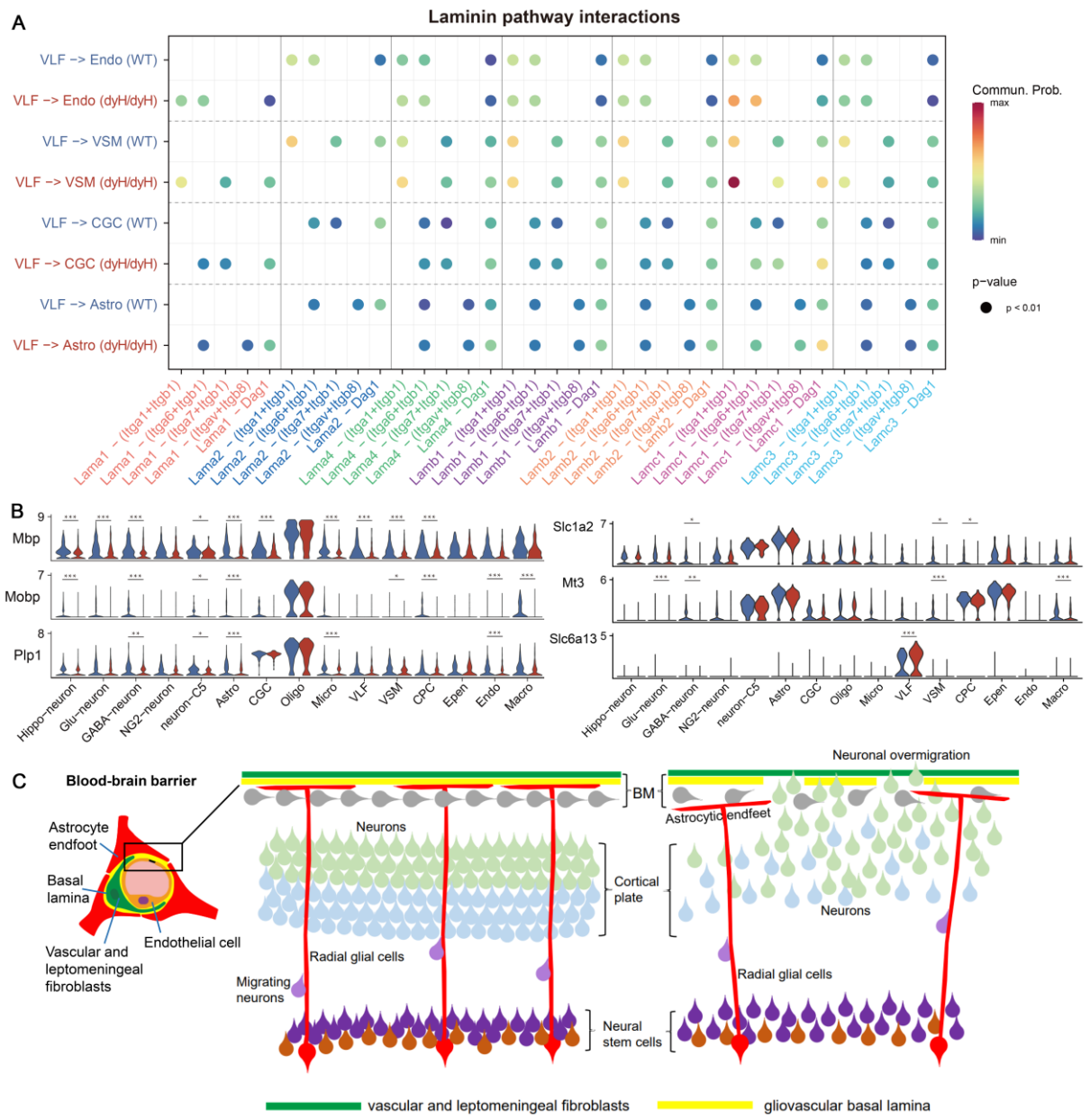

Figure 6. Laminin pathway interactions and hypothesis for cortical dysplasia. (A) The ligand-receptor pairs in laminin pathway. **(B)** Violin plots showed the expression of *Mbp*, *Mobp*, *Plp1*, *Slc1a2*, *Mt3*, and *Slc6a13* in every annotated cell cluster in dy^H/dy^H and WT separately. *** for p-value< 0.001, ** for p-value<0.01, * for p-value<0.05. **(C)** Hypothesis that cortical dysplasia (cobblestone malformation) and neuronal over migration in the cortex due to a defective gliovascular basal lamina of the blood-brain barrier caused by the lack of laminin α2 in *LAMA2*-MD.

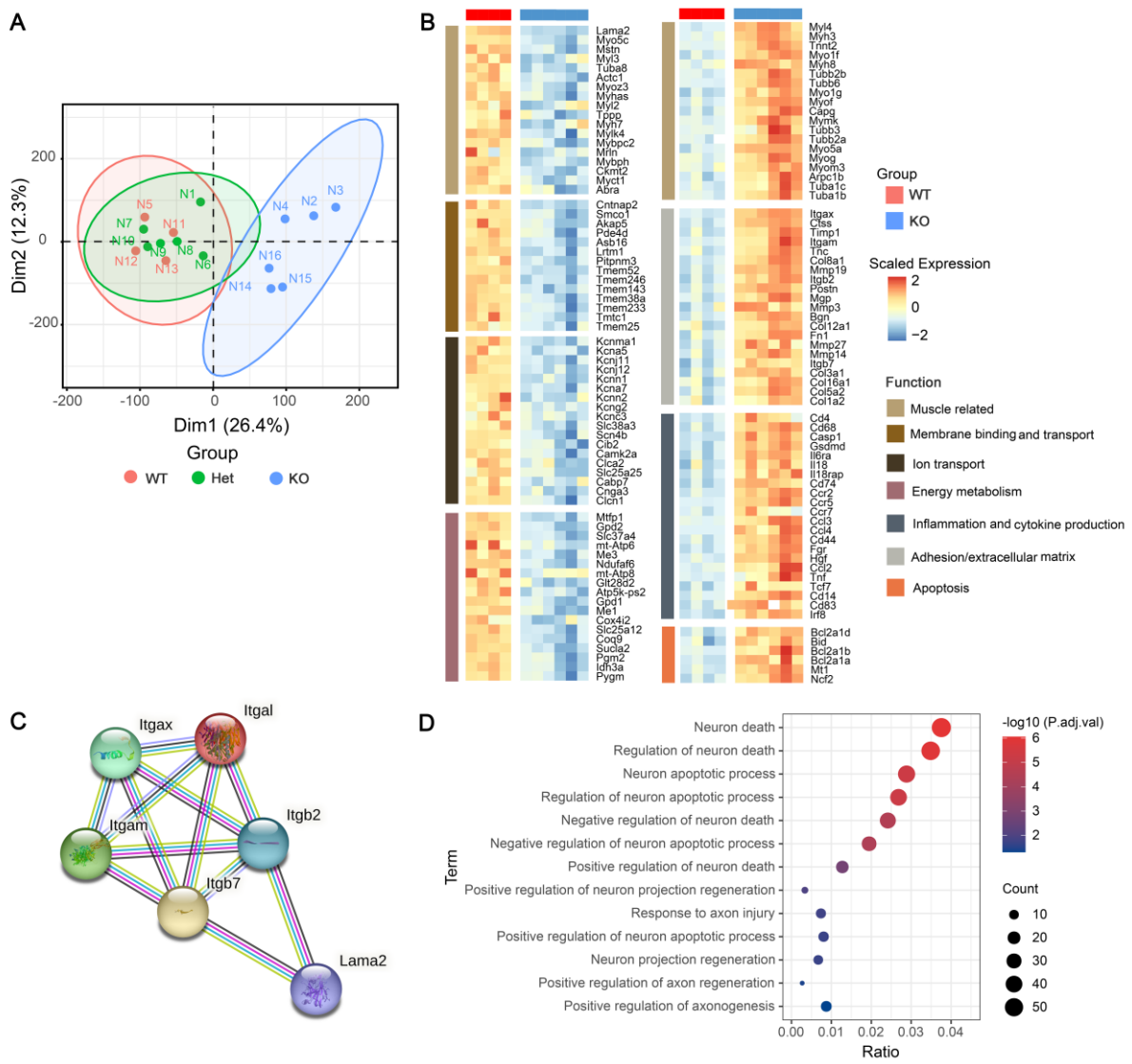

Figure 7. The transcriptional landscape of dy^H/dy^H (KO) mouse muscles in response to wild-type (WT) mouse muscles. (A) Principal component analysis for dimension reduction of differentially expressed genes (DEGs) in the biceps femoris of dy^H/dy^H and dy^H/+ mice in response to WT mice. **(B)** DEGs in dy^H/dy^H muscles relative to WT muscles were enriched in adhesion/extracellular matrix, cytoskeletal proteins and muscle development, ion channel and cell membrane transport, inflammation, mitochondrial metabolism, and apoptosis. **(C)** Protein-protein interactions among *Lama2* and integrins-related genes including *Itgal*, *Itgax*, *Itgam*, *Itgb2*, and *Itgb7*. **(D)** The neuron death related signaling pathways were enriched in dy^H/dy^H muscles relative to WT muscles by GO pathway analyses.

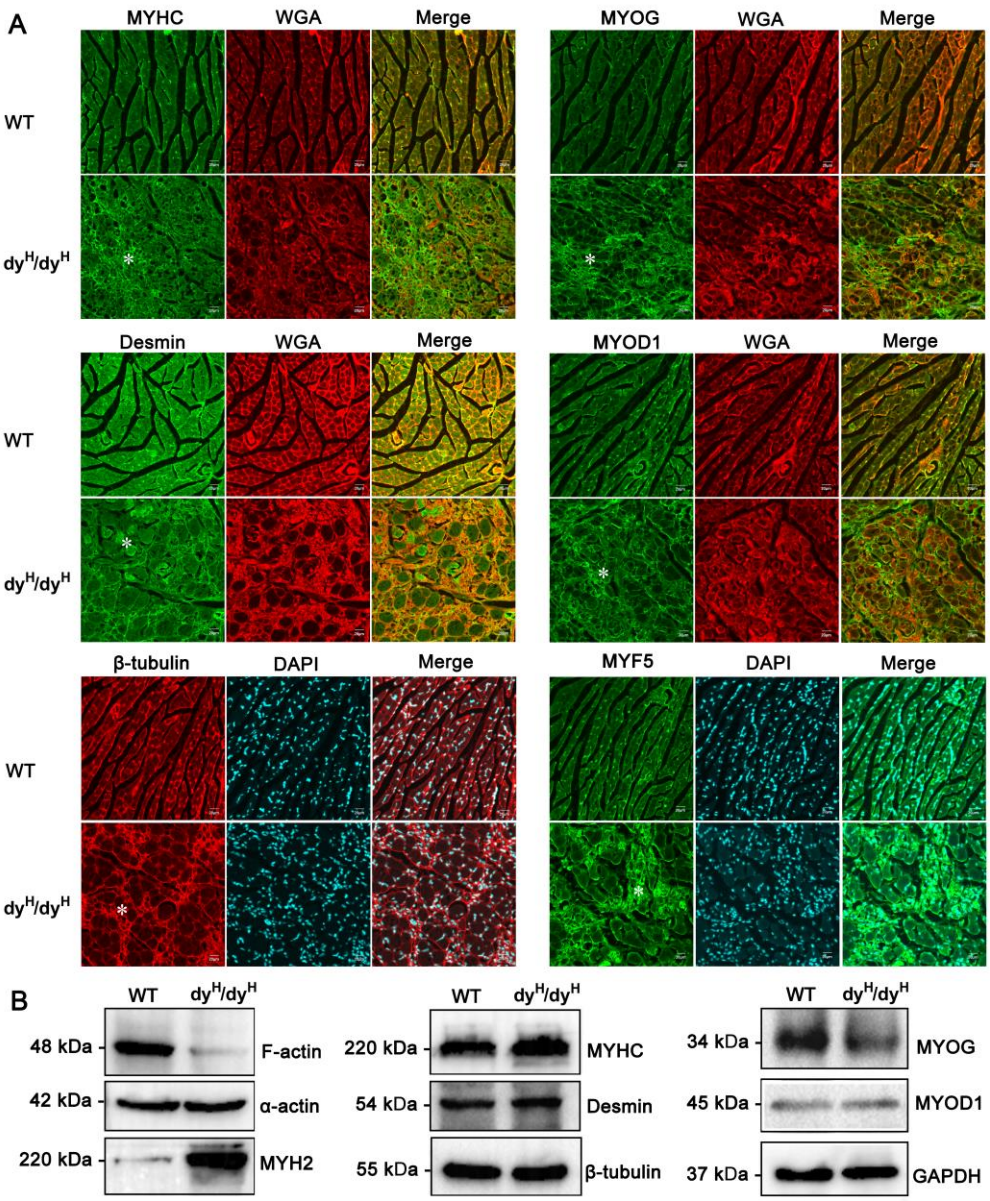

Figure 8. Changes of muscle cytoskeleton and development proteins in dy^H/dy^H mice. (A) Immunofluorescence staining for MYHC, desmin, β-tubulin, MYOG, MYOD1 and MYF-5 in WT and dy^H/dy^H muscles at P14. MYHC, MYOG, MYOD1 and MYF-5 were focally increased, while desmin and β-tubulin showed mild decrease in the cytoplasm of hypertrophic muscle fibers as well as focal increase in developmental muscle fibers in dy^H/dy^H mice. Wheat-germ agglutinin (WGA; red) was used to visualize the muscle fibers and connective tissue. White asterisk indicated focal regions with changes. **(B)** F-actin, α-actin, MYH2, MYHC, desmin, β-tubulin, MYOG and MYOD1 were detected by Western blot in P14 WT (n = 3) and dy^H/dy^H (n = 3) muscles. The levels of F-actin, MYOG and MYOD1 were significantly decreased in dy^H/dy^H muscles ($p < 0.05$), MYH2 and MYHC were significantly increased in dy^H/dy^H muscles ($p < 0.05$), while α-actin, desmin and β-tubulin showed no significant difference between WT (n = 3) and dy^H/dy^H mice.